



Full Length Article

Reoxidation of graphene oxide: Impact on the structure, chemical composition, morphology and dye adsorption properties

Cecilia A. Zito^a, Tarcísio M. Perfecto^a, Talita Mazon^b, Ann-Christin Dippel^c, Dorota Koziej^d, Diogo P. Volanti^{a,*}

^a Laboratory of Materials for Sustainability (LabMatSus), São Paulo State University (UNESP), Rua Cristóvão Colombo 2265, 15054-000 São José do Rio Preto, Brazil

^b Center for Information Technology Renato Archer (CTI), Rod. D. Pedro I, KM 143.6, 13069-901 Campinas, Brazil

^c Deutsches Elektronen-Synchrotron DESY, Notkestrasse 85, 22607 Hamburg, Germany

^d Center for Hybrid Nanostructures (CHyN), Institute of Nanostructure and Solid State Physics, University of Hamburg, Luruper Chaussee 149, 22607 Hamburg, Germany

ARTICLE INFO

Keywords:

Graphite oxide
Total X-ray scattering
Pair distribution function
Cationic dye
Water treatment

ABSTRACT

The chemical composition, oxidation degree, and sheet size strongly affect the properties of graphene oxide (GO). Therefore, much effort has been directed to improve the synthesis of GO and control its structure. Herein, we report the reoxidation of GO using milder conditions of a modified Hummers' method, including shorter reaction times and a reduced proportion of chemicals to obtain the reoxidized GO (Ox-GO). The reoxidation impact was evaluated by studying the materials' adsorption performance towards methylene blue (MB) and rhodamine B (RB). Compared to GO, Ox-GO presents a similar C/O ratio, increased interlayer spacing, smaller sheets with holes, a higher exfoliation degree, and slight differences in each oxygenated functional group. Our measurements evidence that Ox-GO has an MB adsorption capacity more than 30% higher than GO under different conditions of dye concentration and pH. Moreover, Ox-GO also shows a notable improvement in the RB removal for a high dye concentration, where the removal capacity is almost 40% higher than that of GO. The enhancements in the dyes' removal are attributed to the increased accessible surface area of Ox-GO, which provides more sites for dyes' adsorption.

1. Introduction

Graphene oxide (GO) consists of a few layers of carbon atoms with oxygen-containing functional groups [1,2]. The preparation of GO can be carried out by the chemical oxidation of graphite, which results in graphite oxide that is further exfoliated under ultrasonication into a reduced number of layers, then obtaining GO [3]. The production of GO is attractive due to its simplicity, low cost, and high yield [4,5]. Hence, it also provides an economical alternative to obtaining similar properties of graphene by using a subsequent chemical/thermal reduction of GO [6].

The chemical oxidation method introduces several oxygenated functionalities in the structure of graphite that enable the dispersion of GO in water and several solvents [7,8], and allow for surface modification and functionalization [6,9,10]. In this sense, GO is not only widely applied in catalysis [11], sensors [12], fabrication of energy-storage devices [13], and production of composites [14], but it also plays an important role in water treatment. The use of carbon-based

materials, in general, has been widely reported for wastewater purification [15,16], and GO can be applied for the sorption and removal of several contaminants, including dyes [10,17], metal ions [18], radionuclides [19], and aromatic organic compounds [20].

The adsorption ability of GO is closely related to its chemical structure and oxidation degree [21–23]. Depending on the oxidation degree of GO, different affinity and interactions of GO with adsorbates occur, including the preferential zone of interaction [24]. The oxidized zones have an affinity to hydrophilic species, whereas the unoxidized graphitic zones interact with hydrophobic compounds [20,25]. Besides the chemical composition, the GO sheet size also has a tremendous influence on the adsorption properties, mainly due to the specific surface area and active sites for adsorption [23,26]. Therefore, the control of the oxygen content and size of GO sheets can lead to a high adsorption capacity according to the chemical nature of the adsorbates.

In general, much effort has been directed to improve the method to synthesize GO and control its chemical structure and stoichiometry [27–29], leading to new physicochemical properties [30]. An interesting

* Corresponding author.

E-mail address: diogo.volanti@unesp.br (D.P. Volanti).

<https://doi.org/10.1016/j.apsusc.2021.150774>

Received 9 April 2021; Received in revised form 4 July 2021; Accepted 26 July 2021

Available online 28 July 2021

0169-4332/© 2021 Elsevier B.V. All rights reserved.

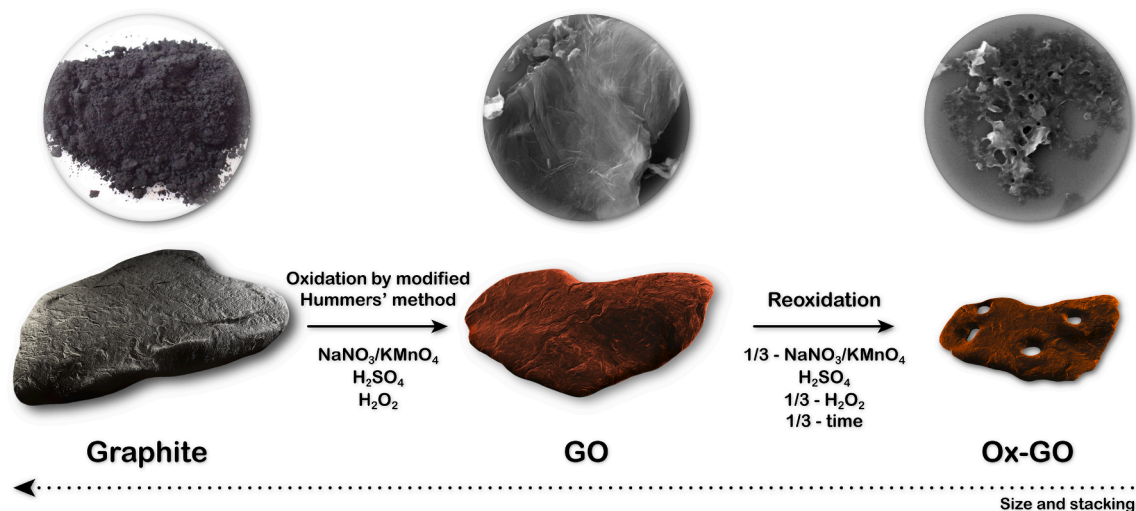


Fig. 1. Schematic illustration for the preparation of Ox-GO via the reoxidation of GO, which is first prepared by a modification of Hummers' method.

approach to obtain unique properties of GO is the reoxidation [31,32]. The reoxidation method drastically increases the overall quantity of oxygen and the concentration of carboxylic acid groups in GO [31–33]. Such enhancement in carboxyl groups can lead to a new graphene derivative material termed graphene acid [32]. The materials resulting from the reoxidation method have better dispersibility and stability in several solvents [32], improved sorption abilities toward metallic ions and gases [31,32], and potential application to produce better membranes for the desalination process [33]. Nevertheless, the reoxidation method is recent and still barely explored in the literature.

Herein, we report the production of reoxidized GO (Ox-GO) by oxidizing pristine GO using milder conditions of a modified Hummers' method that includes shorter reaction times and a reduced amount of chemicals. Our results suggest that rather than introducing more oxygen-containing groups in GO, the reoxidation step reduces the size and stacking of the sheets, increases the interlayer spacing, improves the dispersibility and exfoliation of Ox-GO, and causes only small changes on the type of oxygenated functionalities. As an example of application, we demonstrate the impact of the reoxidation of GO on the adsorption properties towards methylene blue (MB) and rhodamine B (RB), where Ox-GO presents an enhanced adsorption performance compared to GO.

2. Experimental

2.1. Chemicals

Graphite powder (98.0% purity) and NaNO_3 (>99.0% purity) were supplied by Synth. KMnO_4 ($\geq 99.0\%$ purity), H_2SO_4 (95.0–98.0%), and methylene blue ($\geq 82\%$ purity) were distributed by Sigma-Aldrich. H_2O_2 (30%) and rhodamine B ($\geq 99.8\%$ purity) were supplied by Vetec, and HCl (37%) by Fluka Analytical. The chemicals were used as received without additional purification. All experiments were carried out using high purity water with a resistivity of 18.2 $\text{M}\Omega\text{-cm}$ at 25 °C obtained from a Millipore Direct-Q® 3 UV Water Purification System.

2.2. Synthesis of graphite oxide

GO was prepared by a modification of Hummers' method [34] previously reported by our group [35]. According to Hummer's protocol, graphite is treated with oxidants (NaNO_3 and KMnO_4) in fuming H_2SO_4 medium. Briefly, 1.00 g of graphite and 1.00 g of NaNO_3 (1:1 wt ratio) were added to H_2SO_4 (46 mL) and stirred for 30 min in an ice bath at < 5 °C. Subsequently, 6.00 g of KMnO_4 (6 times the weight of graphite) was slowly added, and the mixture was stirred for additional 2 h at a

temperature below 5 °C. The mixture was then heated at ~ 35 °C for 2 h under continuous magnetic stirring. After this period, deionized water (46 mL) was added to the mixture, which was heated at 98 °C for 15 min. Finally, more deionized water (100 mL) and H_2O_2 (20 mL) were added to the mixture to stop the reaction. The product was collected using a centrifuge, washed two times with 1:10 HCl aqueous solution and several times with deionized water, and purified using dialysis for one week. Then, the product was collected and dried at approximately 90 °C overnight. For simplicity, the acronym GO is used for both graphite oxide and graphene oxide throughout the text. Graphene oxide is only obtained after the ultrasonication step; therefore, it is pointed out when the sample is exfoliated using an ultrasonic bath.

2.3. Reoxidation of graphite oxide

The reoxidation of GO was conducted by using milder conditions of the modified Hummers' method. The weights of oxidants and reaction times in each step were reduced by one-third of those in the original conditions. The volumes of deionized water and H_2O_2 in the final stage of the reaction were also decreased by one-third, but the volumes of H_2O , added for the first time in the mixture, and H_2SO_4 were kept the same.

Thus, 1.00 g of GO and 0.3332 g of NaNO_3 (1:0.33 wt ratio) were added to H_2SO_4 (46 mL), and the mixture was stirred for 10 min at < 5 °C. In the sequence, 2.00 g of KMnO_4 (two times the GO weight) was gradually added into the mixture, which was stirred for 40 min at < 5 °C. After this period, the mixture was heated at about 35 °C for 40 min. Then, deionized water (46 mL) was inserted, and the mixture was heated at 98 °C for 5 min. Finally, deionized water (33 mL) and H_2O_2 (6.66 mL) were included. The product was collected, washed 2 times with 1:10 HCl aqueous solution and several times with deionized water, and purified using dialysis. The sample was dried at ~ 90 °C overnight. The sample is labeled Ox-GO. The schematic illustration for the preparation of Ox-GO is depicted in Fig. 1.

2.4. Characterization

Powder X-ray diffraction (PXRD) was performed on a Rigaku Mini-Flex 300 powder diffractometer applying $\text{Cu K}\alpha$ radiation ($\lambda = 1.5418$ Å), which was operated at 30 kV and 10 mA. The samples were scanned in steps of 0.1° at a scan rate of 1° min^{-1} . Attenuated total reflection Fourier transform infrared (ATR-FTIR) spectra were collected using a PerkinElmer Spectrum Two™ spectrometer with a resolution of 2 cm^{-1} . Raman spectroscopy was carried out on a HORIBA T64000 triple grating

spectrometer applying a laser excitation of 633 nm. Field-emission scanning electron microscopy (FESEM) images were taken on a Tescan Mira 3 XMU microscope operated at 10 kV. Atomic force microscopy (AFM) imaging was conducted on a Nanosurf Easyscan 2 microscope. The samples were dispersed on isopropanol, ultrasonicated for 15 min, and dropped on Si substrate for both FESEM and AFM analyses. X-ray photoelectron spectroscopy (XPS) was performed on a Thermo Scientific K-Alpha Spectrometer with an Al K α X-ray radiation source (1486.6 keV). The binding energies were calibrated with reference to the C 1 s peak at 284.8 eV. Elemental analysis was conducted on a PerkinElmer® 2400 Series II CHNS/O Elemental Analyzer, which was operated in the CHN mode. The analysis was conducted three times for each sample using ~ 2.2–2.6 mg. UV/visible spectra were recorded on a Biochrom Libra S60 UV/Vis Spectrophotometer. To perform the analyses, the samples were dispersed in deionized water at a concentration of 0.05 mg mL⁻¹ by using an ultrasonic bath for 30 min. To study the dispersion behavior of the samples in different solvents, ~2 mg of the powders were dispersed in 4 mL of the solvent using ultrasonication (37 kHz, Elmasonic S30H) for 1 h.

Total X-ray scattering data were collected at beamline P07 at PETRA III at Deutsches Elektronen-Synchrotron (DESY), Hamburg, Germany. The 2D diffraction patterns were recorded for 5 min at an energy of 98.2 keV ($\lambda = 0.1263 \text{ \AA}$) using a PerkinElmer XRD1621 detector (2048 × 2048 pixels) at a sample-to-detector distance of 0.437 m. The powders of the samples were packed into Kapton capillaries (inner diameter 1.024 mm) and placed inside a chamber filled with He for the measurements. The calibration for the integration parameters (using the measurements of a LaB₆ standard) and the azimuthal integration of the diffraction patterns were conducted in the pyFAI software [36]. The integrated patterns were background-subtracted employing the data of an empty Kapton capillary, and Fourier transformed to obtain the pair distribution functions (PDFs), $G(r)$, using the PDFgetx3 software [37]. The Q_{\max} parameter, the finite data range applied in the Fourier transform stage, was set to 16.5 \AA^{-1} .

2.5. Dye adsorption tests

All dye adsorption tests were performed at ambient conditions. The concentration of GO or Ox-GO in the experiments was $0.275 \pm 0.010 \text{ mg mL}^{-1}$, whereas the dye concentrations were 200 and 400 mg L⁻¹ for both MB and RB. For the tests, the powder of GO/Ox-GO was first dispersed in deionized water using an ultrasonic bath for 30 min, then mixed with the dye solution. The appropriate volume of each component was adjusted according to the required dye concentration in the reaction, and the final volume of all reactions was 11 mL. The reaction was kept under constant magnetic stirring for 30 min. Finally, the adsorbents were separated from the remaining dye by using centrifugation at 8500 RPM for 4 min. The absorbance of the supernatant was measured and used to determine the dye concentration by using a Biochrom Libra S60 UV/Vis Spectrophotometer. The dye concentrations were determined using the wavelength of 664 nm and 554 nm for MB and RB, respectively. The pH adjustment was performed with HCl or NaOH solutions to study the effect of pH on the adsorption properties. All dye adsorption experiments were conducted two times. The amount of dye adsorbed after 30 min (Q , in mg g⁻¹) was calculated using Eq. (1), and the removal efficiency was calculated by using Eq. (2).

$$Q = \frac{(C_0 - C)V}{m} \quad (1)$$

$$\text{Removal efficiency (\%)} = \left(\frac{C_0 - C}{C_0} \right) \times 100 \quad (2)$$

where C_0 and C (mg L⁻¹) are the concentrations of dye in solution before and after adsorption tests, respectively, V (L) is the volume of the solution, and m is the mass of adsorbent (g).

Table 1

Chemical composition of GO and Ox-GO obtained by elemental CHN analysis.

Sample	C (wt%)	O (wt%)	H (wt%)
GO	45.03 ± 0.67	53.45 ± 0.61	1.52 ± 0.07
Ox-GO	46.17 ± 1.18	52.25 ± 1.11	1.58 ± 0.07

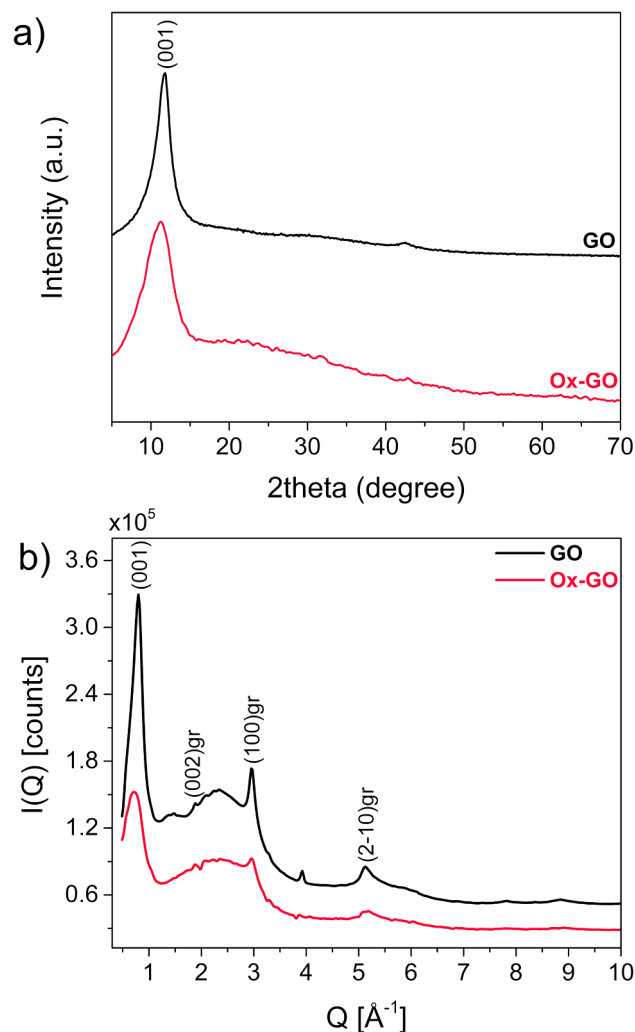


Fig. 2. Structural characterizations of GO, obtained by a modified Hummers' method, and Ox-GO, synthesized via the reoxidation of GO (a) Conventional PXRD patterns. (b) Intensity data $I(Q)$ from total X-ray scattering measurements. The Miller indices are indicated above the reflections, where gr stands for graphite. The (001) reflection corresponds to the interlayer spacing in (a,b).

3. Results and discussion

3.1. Characterization

The reoxidized graphene oxide (Ox-GO) was prepared via the reoxidation of GO using milder conditions of a modified Hummers' method, as shown in Fig. 1. The amounts of oxidants and reaction times were reduced three times compared to those in the original protocol to obtain GO. In the final steps of the synthesis of Ox-GO, the addition of deionized water in the reaction mixture caused the elimination of gas bubbles along with the decrease of the amount of the suspended material in the mixture. This process can be assigned to the partial oxidation of GO in CO₂. Consequently, the resulting mixture at the end of the reaction of Ox-GO is composed of a less dense slurry compared to that of GO (Fig. S1a,b).

Similarly, we tried different milder conditions of the Hummers' method to reoxidize GO by changing some experimental parameters. The scheme of all routes for reoxidation of GO is depicted in Fig. S2. We first reduced by one-third only the reaction times in each synthesis step but the amount of all the chemicals were kept the same. Nevertheless, the synthesis led to a complete transformation of GO into CO₂ and no material remained in the suspension. Afterward, we reduced the reaction times and oxidizing chemicals by half compared to those in the original synthesis of GO. Under such conditions, GO was almost completely oxidized to CO₂, and only a small amount of the material could be collected from the mixture. The final reaction mixture is shown in Fig. S1c, where no material is visible in suspension. Although these two approaches are also milder than the original protocol of Hummers' method, they are unsuccessful and limited due to the decomposition of GO to CO₂. Therefore, the following characterizations were performed only for Ox-GO to be compared to GO.

The chemical compositions of GO and Ox-GO are provided by using elemental CHN analysis, as shown in Table 1. The oxygen (O) concentration is determined by subtracting carbon (C) and hydrogen (H) concentrations from 100%. The results suggest that the chemical composition, *i.e.*, the C/O ratios of both materials are similar. The C/O ratios are about 0.84 and 0.88 for GO and Ox-GO, respectively, indicating that the reoxidation of GO did not introduce more oxygenated functional groups. In fact, the C/O ratio of our pristine GO is already much lower than those for other GOs synthesized *via* the Hummers' method previously reported [31,38,39], which indicates a high oxidation degree. Consequently, the first oxidation to transform graphite in GO is an effective process. We hypothesize that the high degree of oxidation of our pristine GO allows its easy decomposition in CO₂ during the unsuccessful routes of reoxidation of GO.

PXRD analysis is performed to obtain crystallographic information of the materials (Fig. 2a). GO shows the main diffraction peak at 11.75° that corresponds to the interlayer spacing, (001) reflection. Ox-GO presents the same interlayer-related peak but broader and shifted to a lower 2θ value of 11.14°. The interlayer distance is calculated as 7.53 Å for GO and 7.94 Å for Ox-GO, showing that the repeated oxidation increases the interlayer spacing.

Conventional laboratory PXRD techniques can provide structural information from crystalline materials but not from disordered materials. On the other hand, the total X-ray scattering method takes into account the diffuse scattering in addition to the Bragg reflections [40]. It is challenging to obtain high-quality data from disordered materials composed of light elements ($Z < 10$) due to their low X-ray scattering cross-section. However, total X-ray scattering combined with PDF has shown efficiency to characterize such materials [41,42]. So far, limited reports have described GO using total X-ray scattering and PDF analysis. Johnson and co-workers determined the structure of GO by neutron diffraction along with its PDF [43].

The experimental total X-ray scattering data $I(Q)$ for GO and Ox-GO are shown in Fig. 2b. Both samples present similar patterns; nevertheless, the overall intensities of the Ox-GO reflections are lower than those observed in GO. An intense peak at low Q is observed, corresponding to the interlayer spacing (001) reflection that is also observed in the PXRD patterns. The GO peak has its maximum at 0.80 \AA^{-1} that corresponds to the distance of 7.85 Å, whereas Ox-GO shows the broader peak centered at 0.72 \AA^{-1} , representing the interlayer spacing of 8.73 Å. The difference from the values obtained from conventional PXRD can result from the low angular resolution at low angles in total X-ray scattering experiments; however, the results from both techniques confirm the increased interlayer spacing for Ox-GO. Furthermore, the broadening of the interlayer reflection in the $I(Q)$ data of Ox-GO, which is also clear in the PXRD pattern, suggests the presence of different interlayer distances in the material. It has been demonstrated that fluctuations in interlayer spacing in disordered carbons cause a broadening [44,45].

The total X-ray scattering data for both materials also present Bragg peaks related to graphite. The graphite-related reflections are observed

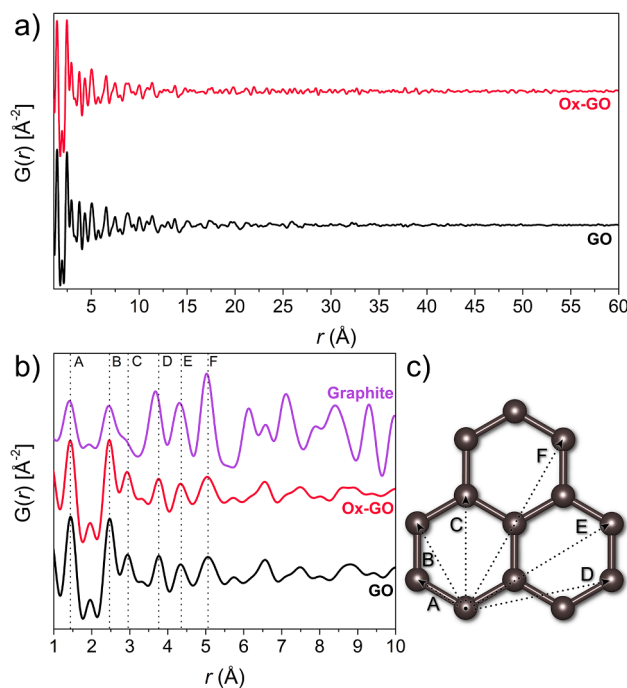


Fig. 3. Experimental PDFs for GO and Ox-GO in the (a) long-range and (b) short-range compared to the simulated PDF of graphite using the crystallographic data from ref. [46], and Q_{\max} of 16.5 \AA^{-1} . (c) Bond distances between carbon atoms in the aromatic ring of graphite for comparison purposes.

at Q values of 1.88, 2.96, and 5.12 \AA^{-1} , assigned respectively to the (002), (100), and (2-10) planes of graphite (gr) (hexagonal structure with $P6_3/mmc$ (194) space group (ICSD: 76767)) [46]. A similar behavior was observed in the neutron diffraction experiments [43]. The graphite-related reflections probably arise from the unoxidized domains (aromatic regions) that remain in the structure of graphite oxide [47], showing that even with the reoxidation step, Ox-GO still presents unoxidized regions in the same way of GO.

The PDF analysis yields the real-space interatomic distances. The experimental PDFs of GO and Ox-GO are shown in Fig. 3a. The PDFs for both materials are similar, where strong correlations are observed at the low r region, and a reduction of correlations occurs beyond 25 Å, suggesting the lack of long-range order beyond this range. Fig. 3b depicts the zoom in the short-range order of the PDFs compared to the simulated PDF of graphite. The peaks seen at 1.44, 2.47 and 2.94 Å correspond to the shortest distances in the ring, whereas the peaks at 3.76, 4.33 and 5.05 Å correspond to the distances to the atoms in the neighboring rings, as depicted in Fig. 3c. Such peaks are shifted and show different relative intensities in GO and Ox-GO compared to the peaks in the simulation of graphite that are observed at 1.41, 2.45, 2.87, 3.67, 4.30, and 5.02 Å. On the one hand, graphite has an ordered structure composed of only carbon atoms in the aromatic rings, whereas GO and Ox-GO contain oxygen functionalities due to the oxidation process that also introduces defects and disorder in the materials' structure. Thus, the shifted peaks might result from the different types of bonds, including C-O bonds and sp^3 carbons (defects) [48]. Both GO and Ox-GO present a small correlation at around 3.33 Å that is not represented in the simulation of graphite, indicating that it is consistent with non-hexagonally bonded carbon distances. This peak suggests a seven-membered ring, as previously shown in PDF studies on different carbon-based materials [42,49]. The value of 3.33 Å is in line with the average value of the C-C distance on opposite sides of a seven-membered ring [49,50]. Moreover, it is not straightforward to match the position of the broad peaks beyond 5 Å in the PDFs of GO and Ox-GO with the peaks in the simulated PDF of graphite, confirming that the oxidation of graphite reduces the ordering in the structure of GO and Ox-GO.

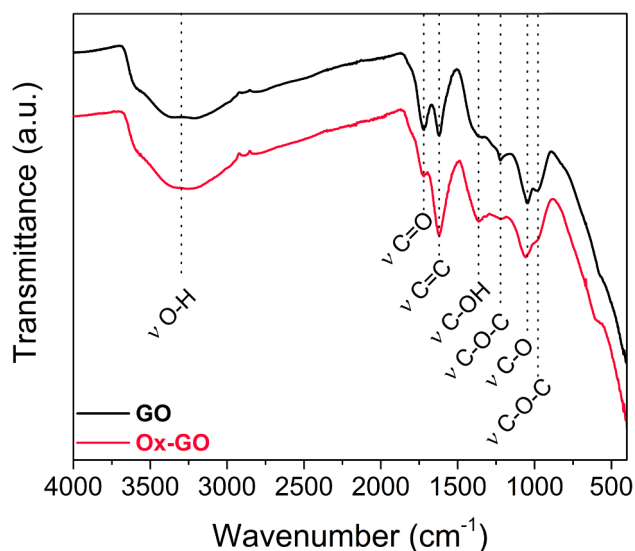


Fig. 4. ATR-FTIR spectra of GO and Ox-GO.

To verify the defects, order, and disorder in the structure of the materials, we perform Raman spectroscopy. As shown in Fig. S3, the Raman spectra of both GO and Ox-GO present two main peaks at 1352 cm^{-1} and 1595 cm^{-1} , corresponding to the D and G bands, respectively. The D band is related to structural defects in the hexagonal framework [51], which can be vacancies, implanted atoms, presence of sp^3 hybridized carbons, and so on [52]. The G band results from the E_{2g} symmetry vibration mode (longitudinal optical (LO) and in-plane transverse optical (TO)) [53] of sp^2 carbons and is related to the graphitic structure. The intensity ratios of the D to G band (I_D/I_G) for GO and Ox-GO are 0.97 and 0.88, respectively. Such a reduction in the I_D/I_G ratio for Ox-GO can be related to the increase in the sp^2 -hybridized domains.

According to the elemental analysis, both GO and Ox-GO have similar C/O ratios; thus, ATR-FTIR spectroscopy is employed to investigate possible changes in their functional groups. The ATR-FTIR spectra in Fig. 4 reveal that both GO and Ox-GO present common features, such

Table 2

Relative quantification in at% of each component in C 1s acquired by high-resolution XPS.

Sample	C—C/C=C	C—O	O—C=O	π - π^*
GO	46.0	43.8	8.6	1.6
Ox-GO	49.4	36.6	12.2	1.8

as the broad band in the range of 3690–2920 cm^{-1} , corresponding to the O—H stretching vibrations from hydroxyl groups and adsorbed water, the peak at around 1047 cm^{-1} (shifted to 1055 cm^{-1} for Ox-GO), which is attributed to the C—O stretching vibration in hydroxyls [31,54], and two features from the C—O stretching vibrations of epoxide groups at 1219 and 980 cm^{-1} [54,55]. However, some differences are also noticed in the spectra after the reoxidation of GO. Both materials show vibration bands at 1720 cm^{-1} and 1620 cm^{-1} , respectively assigned to C=O from carboxyl groups [56] and C=C from the aromatic skeletal [57], but the relative intensities of those peaks change. Ox-GO shows an increase in the intensity of the C=C peak, which agrees well with Raman results. The reoxidation should provide a more oxidized sample, and a more intense peak related to C=O would be expected instead of a peak associated with C=C. Nevertheless, the reoxidation might decompose carboxyl groups and leave more sp^2 carbons in Ox-GO. The decomposition of carboxylic acid has been previously shown in the literature, for instance, when using an excessive amount of H_2O_2 [28]. Finally, Ox-GO presents a more intense peak than GO at 1370 cm^{-1} assigned to tertiary C—OH groups [54,58]. These results suggest that the reoxidation of GO only causes slight changes in the functional groups.

To further differentiate the materials, the surfaces of GO and Ox-GO are characterized by XPS analysis. The survey XPS spectra (Fig. S4) provides a relative quantification of 61.3 at% C and 38.7 at% O for GO, whereas Ox-GO has 62.7 at% C and 37.3 at% O. The C/O ratios are respectively 1.58 and 1.68 for GO and Ox-GO. Thus, the surface composition of both samples is similar, in line with the results of the bulk composition from elemental CHN analysis, confirming that the reoxidation step does not provide a higher content of oxygenated functional groups.

The high-resolution XPS helps to identify the distinct oxygenated functional groups on the surface of both materials. In Fig. 5a, the fitting

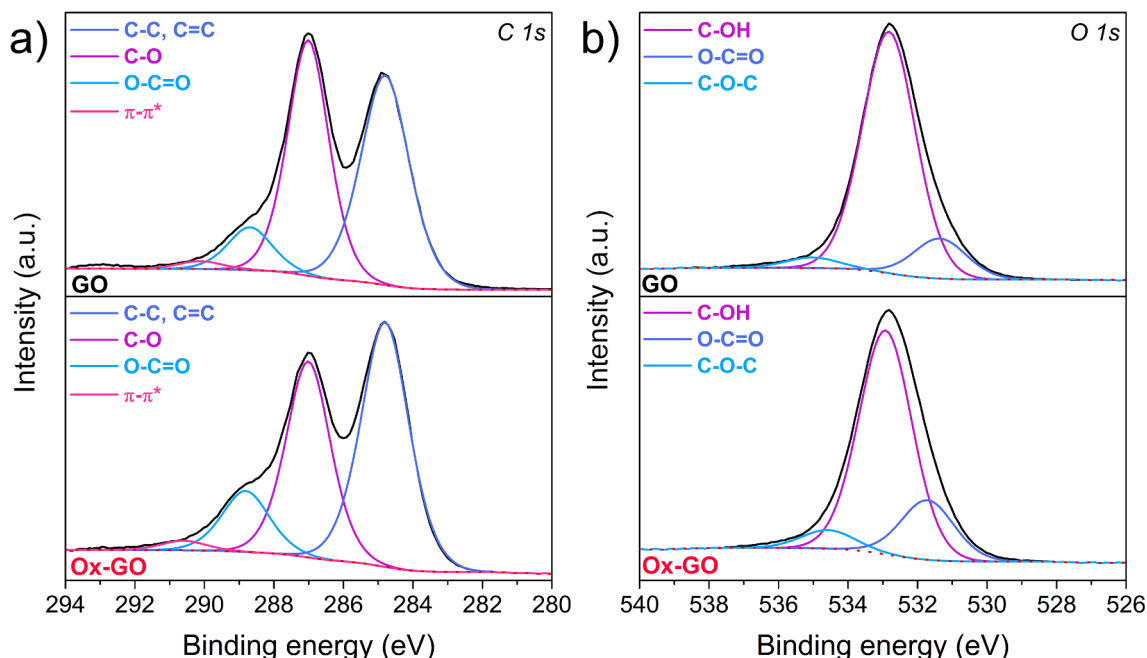


Fig. 5. High-resolution XPS spectra of GO and Ox-GO. Spectra measured at the (a) C 1s energy, and (b) O 1s energy.

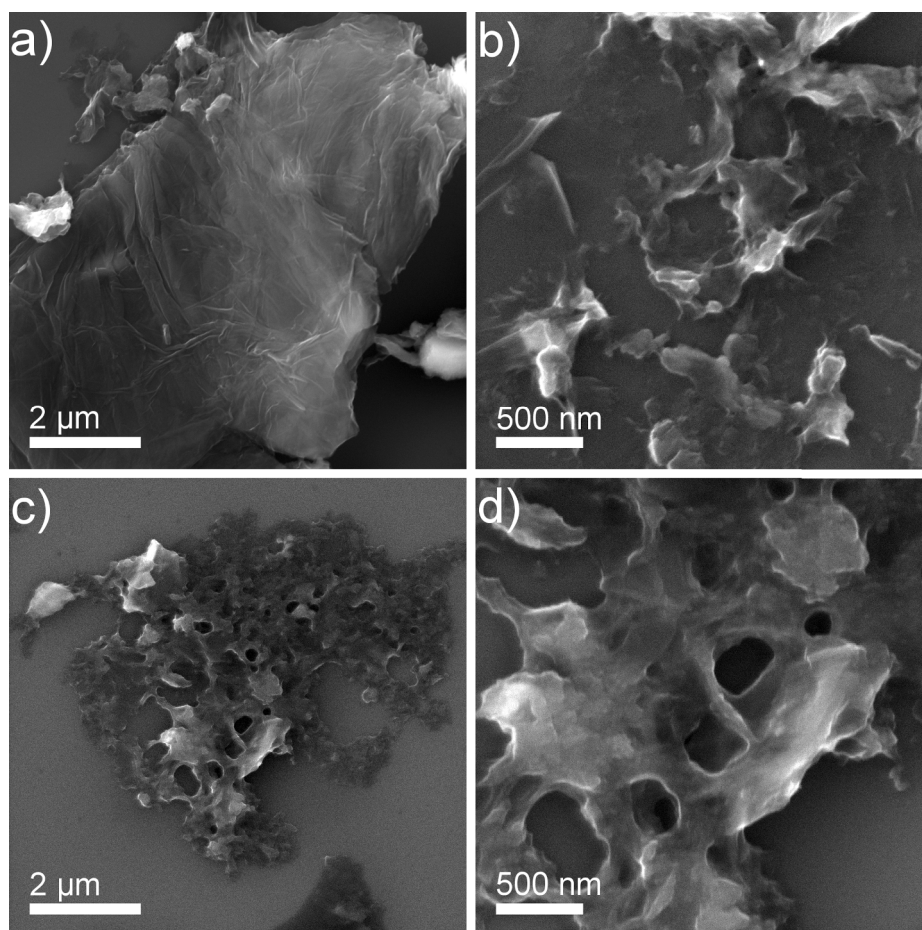


Fig. 6. FESEM images of (a,b) GO, and (c,d) Ox-GO at different magnifications.

of C 1s spectra indicates four components: C=C/C—C (sp^2/sp^3 , 284.8 eV) [13], C—O (287.0 eV) [28,51], O—C=O (288.7 eV for GO, and 288.8 eV for Ox-GO) [51], and $\pi-\pi^*$ interaction (290.1 and 290.6 eV for GO and Ox-GO, respectively) [32]. The relative amounts of the contributions change slightly after the reoxidation of GO, as depicted in Table 2. It is worth mentioning that XPS provides information to a depth of only a few nanometers in the sample and does not represent the whole sample, resulting in different results from those obtained from ATR-FTIR spectroscopy.

The high-resolution O 1s spectra are shown in Fig. 5b. The O 1s spectrum for GO can be resolved into three components O—C=O at 531.3 eV (12.6%), C—OH at 532.8 eV (83.3%), and C—O—C at 534.8 eV (4.1%) [59–61]. Ox-GO also presents three contributions: O—C=O at 531.7 eV (19.7%), C—OH at 532.9 eV (74.1%) and C—O—C at 534.6 eV (6.2%). Therefore, the XPS results suggest that the additional oxidation step does not increase the amount of oxygen on the surface, but the individual contribution of each functional group is slightly different for both materials, as also indicated in ATR-FTIR. Moreover, the higher amount of C=C/C—C in Ox-GO is in line with the decrease in the I_D/I_G ratio observed in the Raman spectra, which suggests an increase in the sp^2 structure.

The UV/Vis spectroscopy confirms the structural differences between GO and Ox-GO, as depicted in Fig. S5. The UV/Vis spectrum of GO shows an absorption peak at 232.8 nm and a shoulder peak at 306.4 nm that correspond respectively to the $\pi \rightarrow \pi^*$ transitions (conjugation) of aromatic C=C bonds and $n \rightarrow \pi^*$ transitions of carbonyl groups (C=O) [8,29]. On the other hand, the spectrum of Ox-GO presents a blue shift to 224.3 nm for the main absorption peak, and no shoulder is observed. The longer λ_{max} for the $\pi \rightarrow \pi^*$ transitions of GO indicates that GO is

more conjugated than Ox-GO [62], possibly due to the larger sheets of GO as discussed below.

Complementary to the structural and chemical characterizations, FESEM analysis provides the morphological information of the samples, as shown in Fig. 6. The FESEM images of GO (Fig. 6a,b and Fig. S6a) elucidate the micrometer-sized sheet that shows a wrinkled surface. Ox-GO also presents micrometer-sized particles with wrinkles (Fig. 6c,d). Nevertheless, there are several holes in the Ox-GO structure, which can provide a higher porosity than GO sheets, and individual smaller particles are also observed, as shown in Fig. S6b. The presence of holes and reduced particle size can result from the removal of functional groups and decomposition of GO in the form of CO_2 during the reoxidation to synthesize Ox-GO.

To further understand the morphological differences between GO and Ox-GO particles, AFM is conducted to obtain information on the thickness of the samples (Fig. S7). AFM analyses suggest that GO has a higher degree of stacking sheets than Ox-GO. On the one hand, the thickness of GO is 4–5 nm, whereas the Ox-GO height is below 3 nm, indicating the more exfoliated sheets. The reduced stacking behavior of Ox-GO can be attributed to the higher interlayer distance that reduces the interactions between the sheets and facilitates exfoliation.

The dispersion behavior of GO and Ox-GO is investigated in different solvents, including protic (water, methanol, ethanol, isopropanol, and ethylene glycol (EG)), aprotic polar (acetone, *N,N*-dimethylformamide (DMF), and dimethyl sulfoxide (DMSO)) and non-polar (chloroform and toluene), as shown in the photographs in Fig. 7. Immediately after the ultrasonication, GO was well dispersed in most of the solvents except chloroform and toluene, and to a lesser extent, acetone. Ox-GO exhibited a similar dispersibility behavior as GO after sonication, although the

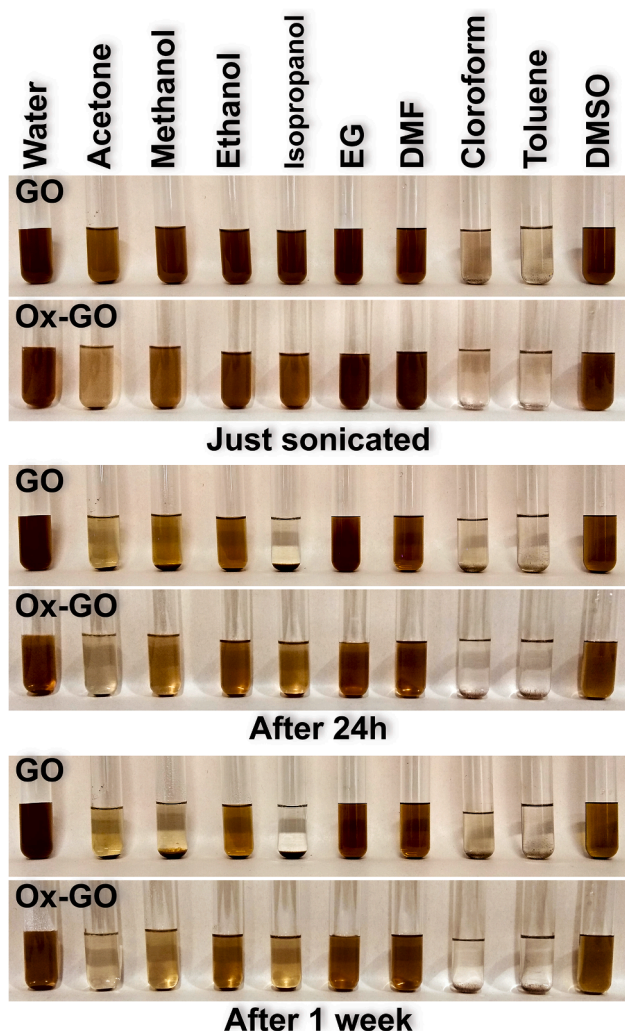


Fig. 7. Photographs of 0.5 mg mL^{-1} dispersions of GO and Ox-GO in different solvents. Immediately after ultrasonication, after 24 h and after one week.

dispersions of Ox-GO presented a slightly lighter brown color compared with those of GO.

The stability of the dispersions was studied after 24 h and one week. The dispersions of GO in water, EG, DMSO, and DMF remained stable after 24 h and an initial precipitation of GO was observed in acetone, methanol, and ethanol, whereas GO was precipitated entirely in isopropanol. The dispersibility of GO remained constant after one week, except in methanol that showed a high degree of precipitation. On the other hand, Ox-GO formed much more long-term stable suspensions than GO. There is no significant difference between the colloidal suspensions after 24 h and one week. Also, less precipitation could be seen, especially in the alcohols. Therefore, Ox-GO not only shows the same dispersibility behavior to GO but has improved long-term stability in more protic solvents, which can be attributed to the smaller particle size and less stacking. Such behavior should enable further manipulation, modifications, and more applications of Ox-GO.

3.2. Dye adsorption performance

To further illustrate the differences between GO and Ox-GO, the materials are applied as adsorbents towards two different dyes, MB and RB. First, the dye adsorption capacities for GO and Ox-GO are evaluated by changing the initial dye concentration. Fig. 8a reveals that the adsorption capacities of Ox-GO for both initial MB concentrations are higher than those of GO. Using an initial MB concentration of 200 mg L^{-1} ,

¹, the amount of dye adsorbed on Ox-GO is 695.36 mg g^{-1} , which is nearly 32% higher than that of GO (527.07 mg g^{-1}). Thus, Ox-GO can adsorb more than 90% of MB, whereas GO adsorbs only 72.2% (Fig. S8a).

When the initial MB concentration increases to 400 mg L^{-1} , the adsorption capacities increase and reach values of 765.54 and 559.47 mg g^{-1} for Ox-GO and GO, respectively. The enhancement of the adsorption capacities might occur due to the facilitation of MB molecules to access the adsorbents' pores when increasing the MB concentration. As shown in FESEM images, Ox-GO has holes in its structures which provides a higher porosity than GO, enabling the improved adsorption of MB. As depicted in Fig. S8a, such adsorption capacities correspond to a removal efficiency equivalent of 53.7% and 39.5% for Ox-GO and GO, respectively, confirming that even for higher concentrations of MB, Ox-GO presents a relatively high adsorption performance. Previous studies used the adsorption of MB to estimate the surface area of graphitic materials, where each 1 mg of adsorbed MB corresponds to an area of 2.54 m^2 [22]. This method can be used as a tool to assume that Ox-GO has a higher surface area than GO.

The behavior of RB adsorption on the materials differs from that of MB. As depicted in Fig. 8b, the amount of dye adsorbed on both materials are remarkably similar when the initial RB concentration is 200 mg L^{-1} , reaching values of 544.90 and 536.96 mg g^{-1} for GO and Ox-GO, respectively. Hence, the removal efficiency of RB of 74.8% for GO and 72.4% for Ox-GO confirms the similarity in the adsorption properties towards RB (Fig. S8b). On the other hand, the difference between the adsorption capacities of GO and Ox-GO increases using an initial RB concentration of 400 mg L^{-1} . For such a high RB concentration, Ox-GO can adsorb 877.75 mg g^{-1} of RB with a removal efficiency of 56.9%, whereas GO adsorbs 636.21 mg g^{-1} (43.0% of removal) that is ca. 38% lower.

It is clear that the adsorption mechanisms towards MB and RB are different, which can be related to the molecular structure of the dyes. The UV/Vis spectra of MB and RB before and after the adsorption tests using GO and Ox-GO, shown in Fig. S9, illustrate the removal efficiency of the adsorbents.

The adsorption mechanism of MB and RB on GO-based materials are mainly based on electrostatic interactions, which causes a charge transfer between adsorbents and adsorbates. The electrostatic interactions with RB may occur in a lower extent than with MB due to the molecular structure of RB that can cause steric hindrance [17]. Previous studies demonstrated a strong and preferential interaction of MB, RB, and other cationic dyes with GO through carboxyl groups [63–65]. Thus, a higher oxidation degree of GO provides a stronger interaction with MB or RB molecules and, consequently, enhanced adsorption since the electrostatic interactions play the main role in the adsorption of these dyes.

Nevertheless, both GO and Ox-GO have nearly the same composition, and Ox-GO even has a lower concentration of carboxylic acid groups than GO, suggesting that the improved adsorption of MB on Ox-GO might not be related to a higher concentration of oxygenated functional groups. The better MB adsorption properties might result from the smaller particles containing holes, the higher degree of exfoliation, and the increased interlayer spacing of Ox-GO. All these factors contribute to increasing the accessible surface area of Ox-GO, providing more active sites for electrostatic interactions with MB molecules. Moreover, the adsorption can also occur via π - π interactions of the sp^2 carbons in the adsorbents with the aromatic rings of the dyes [64], but on a smaller scale due to the existence of several oxygenated functional groups in GO derivatives. Consequently, the higher concentration of $\text{C}=\text{C}$ bonds in Ox-GO might also contribute to its improved MB removal performance.

On the other hand, such characteristics of Ox-GO did not aid in enhancing the RB adsorption compared to GO for the low dye concentration. At low RB concentration, the access of the RB molecules into the pores of both GO and Ox-GO occurs similarly. However, when the RB concentration increases, the higher accessibility to the pores in Ox-GO

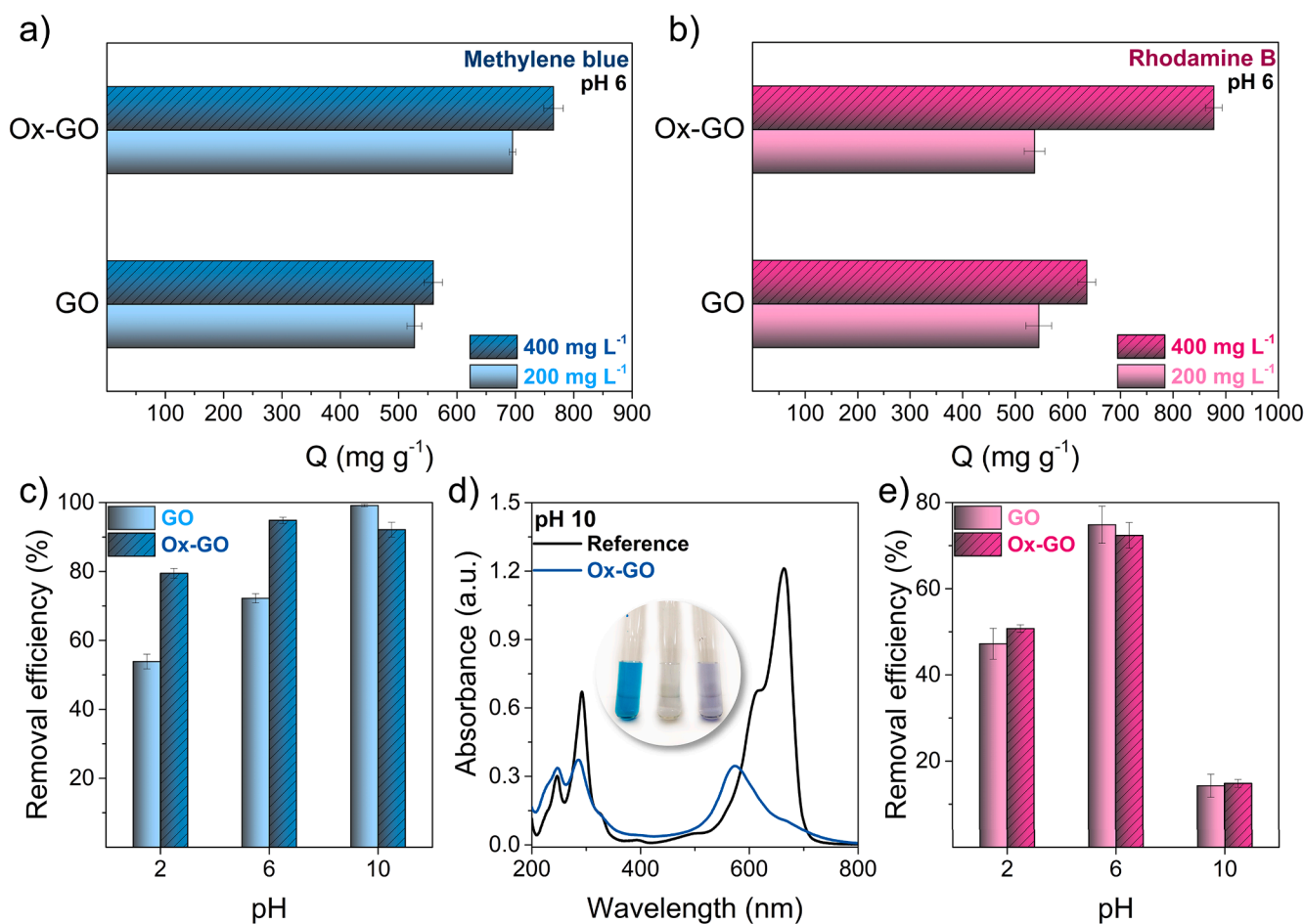


Fig. 8. Adsorption performance of GO and Ox-GO towards MB and RB. (a,b) Adsorption capacities of GO and Ox-GO towards (a) MB, and (b) RB, changing the initial concentration of the dyes (200 and 400 mg L⁻¹). The pH of the solution is 6, and the contact time for adsorption is 30 min. (c) Effect of initial solution pH on the removal efficiency towards MB, using an initial MB concentration of 200 mg L⁻¹. (d) Comparison of the UV/Vis spectra of the reference MB solution at 200 mg L⁻¹ and the supernatant after adsorption experiment using Ox-GO with an initial MB concentration of 200 mg L⁻¹. Both spectra were measured at pH 10, and the solutions were diluted 26 times before recording both spectra. The photograph in the inset shows from left to right the MB reference solution, the supernatant of GO experiment, and the supernatant of Ox-GO experiment. All three solutions were also diluted 26 times. (e) Effect of initial solution pH on the removal efficiency towards RB, using an initial RB concentration of 200 mg L⁻¹.

results in the notably enhanced adsorption performance.

The adsorption process depends on the pH of the solution due to the changes in the charge/species of the dye and the surface charge of the adsorbent. The role of the solution pH on the MB adsorption behavior is studied, as depicted in Fig. 8c. The reduction in the solution pH from the natural value of 6 to 2 causes a decrease in the removal efficiency for both GO and Ox-GO. The lower removal abilities at pH 2 can be a result of the decrease in the electrostatic interactions between the adsorbents and MB. Nevertheless, Ox-GO still presents a superior adsorption performance, removing ca. 79.5% of MB from the solution that corresponds to a 47% improved efficiency compared to that of GO.

The removal efficiency of GO reaches almost 100% with increasing the pH to 10. The increase in the adsorption capacities with increasing the pH can be attributed to the enhancement in the negative charges in GO due to the deprotonation of anionic groups at higher pH values [24]. Consequently, GO presents a higher affinity to cationic dyes like MB with increasing pH and higher adsorption performance [17].

However, Ox-GO shows a completely distinct behavior compared to GO at pH 10. The UV/Vis spectrum of the supernatant after the adsorption tests using Ox-GO as adsorbent shows a shift in the maximum absorption wavelength to ~573 nm (*versus* 664 nm of MB), as well as different intensities of the peaks in the region of 200–340 nm compared to MB (Fig. 8d). As depicted in the inset of Fig. 8d, the blue solution of MB turns into a violet supernatant after the adsorption experiments

using Ox-GO, whereas the supernatant from GO tests is colorless. Previous studies demonstrated the transformation of MB under alkaline conditions into other related dye substances, such as methylene violet that has a maximum absorbance at 580 nm [66,67]. The MB reference solution at pH 10 still shows the characteristic spectrum of MB without any changes, while GO removes almost all MB from the solution, but the small remaining dye in the solution has the characteristic spectrum of MB (Fig. S10). Thus, we can assume that Ox-GO not only adsorbs a certain amount of dye (either in modified or original form) but also aids in transforming MB into other species in such a short time of 30 min. The precise mechanism of the role of Ox-GO under alkali conditions in removing and transforming MB exceeds the scope of this contribution, but it confirms how GO and Ox-GO present distinct properties. It is worth noting that the value of the removal efficiency of MB for Ox-GO at pH 10 is not accurate due to the dye transformation.

The removal efficiency for RB at different pH is shown in Fig. 8e. The removal efficiencies for GO and Ox-GO are very similar at all pH range, but Ox-GO shows a slightly improved performance at pH 2 and 10. The adsorption performances of both adsorbents decrease ~20–27% when reducing the pH to 2. This behavior can be explained by the lower extent of deprotonation of functional groups in the adsorbents at such a low pH, reducing the interactions with RB, which is in a cationic form. The removal efficiencies are further reduced at pH 10 and reach values of only ~14%. RB has a carboxylic acid that dissociates at higher pH and

provides a negative charge on the dye [17], resulting in electrostatic repulsions with GO/Ox-GO (negatively charged at pH 10). Therefore, the optimized pH for RB removal is 6. The adsorption capacities in removing MB and RB are depicted in Fig. S11.

To summarize, our studies show that the adsorption properties depend not only on the structure of the adsorbent materials but also on the dye properties. On the one hand, Ox-GO shows an improved MB removal performance under different conditions such as low and high dye concentrations and acid pH, whereas the enhanced removal of RB only occurs for high concentrations of the dye. The improved adsorption capacity is usually attributed to the higher oxidation degree of the GO [24]. However, here, we show that the degree of oxidation of GO and Ox-GO are similar, suggesting that the improved performance of Ox-GO is related to the improved accessible surface area for interactions due to the higher exfoliation degree, larger interlayer spacing, reduced sheet sizes, active sites, and porosity.

4. Conclusions

In summary, we present the reoxidation of GO by using milder conditions of a modified Hummers' method to obtain Ox-GO. We show that the reoxidation step does not lead to an increased content of oxygenated groups but instead, it causes only a small change in the concentration of each functionality, increases the interlayer spacing, reduces the sheet size, introduces holes in the sheets, facilitates the exfoliation, and improves the long-term stability of the dispersions in protic solvents.

As a possible application of the materials, we investigate their dye removal efficiency. Our measurements evidence that Ox-GO has an MB adsorption capacity more than 30% higher than GO under different conditions of dye concentration and pH. Moreover, unlike pristine GO, Ox-GO can play a role in converting MB into different species under alkaline conditions. The experiments on the removal of RB show that both GO and Ox-GO present similar efficiency, except for a high RB concentration, where Ox-GO shows an almost 40% improved removal capacity due to the presence of holes in its structure. Thus, the reoxidation step of GO is an efficient approach to produce a material with enhanced dye adsorption properties, enabling the application in water treatment. Moreover, Ox-GO can also be used for the adsorption of gases or metallic ions, has potential application in synthetic transformations [68,69], and can be used to produce composites.

CRediT authorship contribution statement

Cecilia A. Zito: Conceptualization, Methodology, Validation, Investigation, Writing – original draft. **Tarcisio M. Perfecto:** Methodology, Validation, Investigation, Writing - review & editing. **Talita Mazon:** Validation, Investigation, Writing - review & editing. **Ann-Christin Dippel:** Investigation, Writing - review & editing. **Dorota Koziej:** Writing - review & editing, Funding acquisition. **Diogo P. Volanti:** Writing - review & editing, Supervision, Project administration, Funding acquisition.

Declaration of Competing Interest

The authors declare that they have no known competing financial interests or personal relationships that could have appeared to influence the work reported in this paper.

Acknowledgments

We thank the São Paulo Research Foundation (FAPESP; grants 2018/08271-7, 2016/25267-8, 2018/00033-0, 2020/06421-1, 2017/01267-1), National Council for Scientific and Technological Development (CNPq, grant 308327/2018-7), and the financial support by the Federal Ministry of Education and Research of Germany (BMBF) in the

framework of LUCENT (Project 05K19GU7). We acknowledge the Multi-user Laboratory for Advanced Optical Spectroscopy – LMEQO/IQ/UNICAMP for Raman facilities and the Brazilian Nanotechnology National Laboratory – LNNano/CNPq (proposals 23272 and 24622) for the XPS facilities. Research supported by CTI's Open Labs - Multiple Users and Shared Facilities, CTI Renato Archer, research institution from MCTI. Research supported by CTI-Nano, strategic laboratory from Sis-Nano, MCTI and financed by CNPq and FAPESP (CEPID-CDMF 2013/07296-2). Parts of this research were carried out at P07 beamline at PETRA III at DESY (Hamburg, Germany), a member of the Helmholtz Association HGF, and we would like to thank the beamline staff, especially Olof Gutowski, for the assistance in the experiments. We also acknowledge Giovana M. Galvani for the assistance with the adsorption experiments.

Appendix A. Supplementary material

Supplementary data to this article can be found online at <https://doi.org/10.1016/j.apsusc.2021.150774>.

References

- [1] S.C. Ray, Application and uses of graphene oxide and reduced graphene oxide, in: *Appl. Graphene Graphene-Oxide Based Nanomater*, Elsevier, 2015, pp. 39–55, <https://doi.org/10.1016/B978-0-323-37521-4.00002-9>.
- [2] A. Ganguly, S. Sharma, P. Papakonstantinou, J. Hamilton, Probing the thermal deoxygenation of graphene oxide using high-resolution in situ X-ray-based spectroscopies, *J. Phys. Chem. C*. 115 (34) (2011) 17009–17019, <https://doi.org/10.1021/jp203741y>.
- [3] C.N.R. Rao, A.K. Sood, K.S. Subrahmanyam, A. Govindaraj, Graphene: the new two-dimensional nanomaterial, *Angew. Chemie Int. Ed.* 48 (42) (2009) 7752–7777, <https://doi.org/10.1002/anie.v48:4210.1002/anie.200901678>.
- [4] M. Khan, M.N. Tahir, S.F. Adil, H.U. Khan, M.R.H. Siddiqui, A.A. Al-warthan, W. Tremel, Graphene based metal and metal oxide nanocomposites: synthesis, properties and their applications, *J. Mater. Chem. A*. 3 (37) (2015) 18753–18808, <https://doi.org/10.1039/C5TA02240A>.
- [5] R. Raccichini, A. Varzi, S. Passerini, B. Scrosati, The role of graphene for electrochemical energy storage, *Nat. Mater.* 14 (3) (2015) 271–279, <https://doi.org/10.1038/nmat4170>.
- [6] A.T. Smith, A.M. LaChance, S. Zeng, B. Liu, L. Sun, Synthesis, properties, and applications of graphene oxide/reduced graphene oxide and their nanocomposites, *Nano Mater. Sci.* 1 (1) (2019) 31–47, <https://doi.org/10.1016/j.nanoms.2019.02.004>.
- [7] D. Konios, M.M. Stylianakis, E. Stratakis, E. Kymakis, Dispersion behaviour of graphene oxide and reduced graphene oxide, *J. Colloid Interface Sci.* 430 (2014) 108–112, <https://doi.org/10.1016/j.jcis.2014.05.033>.
- [8] J.I. Paredes, S. Villar-Rodil, A. Martínez-Alonso, J.M.D. Tascón, Graphene oxide dispersions in organic solvents, *Langmuir*. 24 (19) (2008) 10560–10564, <https://doi.org/10.1021/la801744a>.
- [9] K. Ma, R. Wang, T. Jiao, J. Zhou, L. Zhang, J. Li, Z. Bai, Q. Peng, Preparation and aggregate state regulation of co-assembly graphene oxide-porphyrin composite Langmuir films via surface-modified graphene oxide sheets, *Colloids Surfaces A Physicochem. Eng. Asp.* 584 (2020) 124023, <https://doi.org/10.1016/j.colsurfa.2019.124023>.
- [10] R. Zambare, X. Song, S. Bhuvana, J.S. Antony Prince, P. Nemade, Ultrafast dye removal using ionic liquid-graphene oxide sponge, *ACS Sustain. Chem. Eng.* 5 (7) (2017) 6026–6035, <https://doi.org/10.1021/acssuschemeng.7b00867>.
- [11] H. Sun, S. Liu, G. Zhou, H.M. Ang, M.O. Tadó, S. Wang, Reduced graphene oxide for catalytic oxidation of aqueous organic pollutants, *ACS Appl. Mater. Interfaces*. 4 (10) (2012) 5466–5471, <https://doi.org/10.1021/am301372d>.
- [12] Y.V. Stebunov, O.A. Aftenieva, A.V. Arsenin, V.S. Volkov, Highly sensitive and selective sensor chips with graphene-oxide linking layer, *ACS Appl. Mater. Interfaces*. 7 (39) (2015) 21727–21734, <https://doi.org/10.1021/acsami.5b04427>.
- [13] S.-H. Park, H.-K. Kim, S.-B. Yoon, C.-W. Lee, D. Ahn, S.-I. Lee, K.C. Roh, K.-B. Kim, Spray-assisted deep-frying process for the in situ spherical assembly of graphene for energy-storage devices, *Chem. Mater.* 27 (2) (2015) 457–465, <https://doi.org/10.1021/cm5034244>.
- [14] C.A. Zito, T.M. Perfecto, C.S. Fonseca, D.P. Volanti, Effective reduced graphene oxide sheets/hierarchical flower-like NiO composites for methanol sensing under high humidity, *New J. Chem.* 42 (11) (2018) 8638–8645, <https://doi.org/10.1039/C8NJ01061G>.
- [15] S. Ye, G. Zeng, X. Tan, H. Wu, J. Liang, B. Song, N. Tang, P. Zhang, Y. Yang, Q. Chen, X. Li, Nitrogen-doped biochar fiber with graphitization from Boehmeria nivea for promoted peroxymonosulfate activation and non-radical degradation pathways with enhancing electron transfer, *Appl. Catal. B Environ.* 269 (2020) 118850, <https://doi.org/10.1016/j.apcatb.2020.118850>.
- [16] S. Ye, M. Cheng, G. Zeng, X. Tan, H. Wu, J. Liang, M. Shen, B. Song, J. Liu, H. Yang, Y. Zhang, Insights into catalytic removal and separation of attached metals from

- natural-aged microplastics by magnetic biochar activating oxidation process, *Water Res.* 179 (2020) 115876, <https://doi.org/10.1016/j.watres.2020.115876>.
- [17] G.K. Ramesha, A. Vijaya Kumara, H.B. Muralidhara, S. Sampath, Graphene and graphene oxide as effective adsorbents toward anionic and cationic dyes, *J. Colloid Interface Sci.* 361 (1) (2011) 270–277, <https://doi.org/10.1016/j.jcis.2011.05.050>.
- [18] L. Chaabane, E. Beyou, A. El Ghali, M.H.V. Baouab, Comparative studies on the adsorption of metal ions from aqueous solutions using various functionalized graphene oxide sheets as supported adsorbents, *J. Hazard. Mater.* 389 (2020) 121839, <https://doi.org/10.1016/j.jhazmat.2019.121839>.
- [19] A.S. Kuzenkova, A.Y. Romanchuk, A.L. Trigub, K.I. Maslakov, A.V. Egorov, L. Amidani, C. Kittrell, K.O. Kvashnina, J.M. Tour, A.V. Talyzin, S.N. Kalmykov, New insights into the mechanism of graphene oxide and radionuclide interaction, *Carbon N. Y.* 158 (2020) 291–302, <https://doi.org/10.1016/j.carbon.2019.10.003>.
- [20] H. Yan, H.u. Wu, K. Li, Y. Wang, X. Tao, H.u. Yang, A. Li, R. Cheng, Influence of the surface structure of graphene oxide on the adsorption of aromatic organic compounds from water, *ACS Appl. Mater. Interfaces.* 7 (12) (2015) 6690–6697, <https://doi.org/10.1021/acsami.5b00053>.
- [21] P. Tan, Q. Bi, Y. Hu, Z. Fang, Y. Chen, J. Cheng, Effect of the degree of oxidation and defects of graphene oxide on adsorption of Cu²⁺ from aqueous solution, *Appl. Surf. Sci.* 423 (2017) 1141–1151, <https://doi.org/10.1016/j.apsusc.2017.06.304>.
- [22] N. Morimoto, T. Kubo, Y. Nishina, Tailoring the oxygen content of graphite and reduced graphene oxide for specific applications, *Sci. Rep.* 6 (2016) 21715, <https://doi.org/10.1038/srep21715>.
- [23] S.P. Lee, G.A.M. Ali, H. Algarni, K.F. Chong, Flake size-dependent adsorption of graphene oxide aerogel, *J. Mol. Liq.* 277 (2019) 175–180, <https://doi.org/10.1016/j.molliq.2018.12.097>.
- [24] H. Yan, X. Tao, Z. Yang, K. Li, H. Yang, A. Li, R. Cheng, Effects of the oxidation degree of graphene oxide on the adsorption of methylene blue, *J. Hazard. Mater.* 268 (2014) 191–198, <https://doi.org/10.1016/j.jhazmat.2014.01.015>.
- [25] W. Ren, H. Chang, T. Mao, Y. Teng, Planarity effect of polychlorinated biphenyls adsorption by graphene nanomaterials: The influence of graphene characteristics, solution pH and temperature, *Chem. Eng. J.* 362 (2019) 160–168, <https://doi.org/10.1016/j.cej.2019.01.027>.
- [26] X. Liu, J. Sun, X. Xu, A. Alsaedi, T. Hayat, J. Li, Adsorption and desorption of U(VI) on different-size graphene oxide, *Chem. Eng. J.* 360 (2019) 941–950, <https://doi.org/10.1016/j.cej.2018.04.050>.
- [27] J. Chen, F. Chi, L. Huang, M. Zhang, B. Yao, Y. Li, C. Li, G. Shi, Synthesis of graphene oxide sheets with controlled sizes from sieved graphite flakes, *Carbon N. Y.* 110 (2016) 34–40, <https://doi.org/10.1016/j.carbon.2016.08.096>.
- [28] M.J. Yoo, H.B. Park, Effect of hydrogen peroxide on properties of graphene oxide in Hummers method, *Carbon N. Y.* 141 (2019) 515–522, <https://doi.org/10.1016/j.carbon.2018.10.009>.
- [29] D.C. Marcano, D.V. Kosynkin, J.M. Berlin, A. Sinitskii, Z. Sun, A. Slesarev, L. B. Alemany, W. Lu, J.M. Tour, Improved synthesis of graphene oxide, *ACS Nano.* 4 (8) (2010) 4806–4814, <https://doi.org/10.1021/nn1006368>.
- [30] P. Heydari, A. Hafizi, M.R. Rahimpour, R. Khalifeh, Experimental investigation of improved graphene oxide as an efficient catalyst for the sustainable chemical fixation of CO₂ with epoxides, *J. Environ. Chem. Eng.* 8 (6) (2020) 104568, <https://doi.org/10.1016/j.jece.2020.104568>.
- [31] M. Nováček, O. Jankovský, J. Luxa, D. Sedmidubský, M. Pumera, V. Fila, M. Lhotka, K. Klímová, S. Matějková, Z. Sofer, Tuning of graphene oxide composition by multiple oxidations for carbon dioxide storage and capture of toxic metals, *J. Mater. Chem. A.* 5 (6) (2017) 2739–2748, <https://doi.org/10.1039/C6TA03631G>.
- [32] O. Jankovský, M. Nováček, J. Luxa, D. Sedmidubský, V. Fila, M. Pumera, Z. Sofer, A new member of the graphene family: graphene acid, *Chem. - A Eur. J.* 22 (48) (2016) 17416–17424, <https://doi.org/10.1002/chem.201603766>.
- [33] H. Khorramdel, E. Dabiri, F.F. Tabrizi, M. Galehdari, Synthesis and characterization of graphene acid membrane with ultrafast and selective water transport channels, *Sep. Purif. Technol.* 212 (2019) 497–504, <https://doi.org/10.1016/j.seppur.2018.11.044>.
- [34] W.S. Hummers, R.E. Offeman, Preparation of graphitic oxide, *J. Am. Chem. Soc.* 80 (1958) 1339, <https://doi.org/10.1021/ja01539a017>.
- [35] T.M. Perfecto, C.A. Zito, D.P. Volanti, Room-temperature volatile organic compounds sensing based on WO₃·0.33H₂O, hexagonal-WO₃, and their reduced graphene oxide composites, *RSC Adv.* 6 (107) (2016) 105171–105179, <https://doi.org/10.1039/C6RA16892B>.
- [36] G. Ashiotis, A. Deschildre, Z. Nawaz, J.P. Wright, D. Karkoulis, F.E. Picca, J. Kieffer, The fast azimuthal integration Python library: PyFAI, *J. Appl. Crystallogr.* 48 (2015) 510–519, <https://doi.org/10.1107/S1600576715004306>.
- [37] P. Juhás, T. Davis, C.L. Farrow, S.J.L. Billinge, PDFgetX3: A rapid and highly automatable program for processing powder diffraction data into total scattering pair distribution functions, *J. Appl. Crystallogr.* 46 (2) (2013) 560–566, <https://doi.org/10.1107/S0021889813005190>.
- [38] E.M. Aliyev, M.M. Khan, A.M. Nabiye, R.M. Alosmanov, I.A. Bunyad-zadeh, S. Shishatskiy, V. Filiz, Covalently modified graphene oxide and polymer of intrinsic microporosity (PIM-1) in mixed matrix thin-film composite membranes, *Nanoscale Res. Lett.* 13 (2018) 359, <https://doi.org/10.1186/s11671-018-2771-3>.
- [39] A. Alkhouzaim, H. Qiblawey, M. Khraisheh, M. Atieh, M. Al-Ghouti, Synthesis of graphene oxides particle of high oxidation degree using a modified Hummers method, *Ceram. Int.* 46 (15) (2020) 23997–24007, <https://doi.org/10.1016/j.ceramint.2020.06.177>.
- [40] P.J. Chupas, X. Qiu, J.C. Hanson, P.L. Lee, C.P. Grey, S.J.L. Billinge, Rapid-acquisition pair distribution function (RA-PDF) analysis, *J. Appl. Crystallogr.* 36 (6) (2003) 1342–1347, <https://doi.org/10.1107/S0021889803017564>.
- [41] V. Petkov, Y. Ren, S. Kabekkodu, D. Murphy, Atomic pair distribution functions analysis of disordered low-Z materials, *Phys. Chem. Chem. Phys.* 15 (22) (2013) 8544, <https://doi.org/10.1039/c2cp43378h>.
- [42] J.K. Mathiesen, R. Väli, M. Härmas, E. Lust, J. F. Old von Bülow, K.M.Ø. Jensen, P. Norby, Following the in-plane disorder of sodiated hard carbon through operando total scattering, *J. Mater. Chem. A.* 7 (19) (2019) 11709–11717, <https://doi.org/10.1039/C9TA02413A>.
- [43] J.A. Johnson, C.J. Benmore, S. Stankovich, R.S. Ruoff, A neutron diffraction study of nano-crystalline graphite oxide, *Carbon N. Y.* 47 (9) (2009) 2239–2243, <https://doi.org/10.1016/j.carbon.2009.04.016>.
- [44] K. Jurkiewicz, M. Pawlyta, A. Burian, Structure of carbon materials explored by local transmission electron microscopy and global powder diffraction probes, *C.* 4 (2018) 68, <https://doi.org/10.3390/c4040068>.
- [45] C.R. Houska, B.E. Warren, X-Ray study of the graphitization of carbon black, *J. Appl. Phys.* 25 (12) (1954) 1503–1509, <https://doi.org/10.1063/1.1702373>.
- [46] P. Trucano, R. Chen, Structure of graphite by neutron diffraction, *Nature.* 258 (5531) (1975) 136–137, <https://doi.org/10.1038/258136a0>.
- [47] H. He, J. Klinowski, M. Forster, A. Lerf, A new structural model for graphite oxide, *Chem. Phys. Lett.* 287 (1–2) (1998) 53–56, [https://doi.org/10.1016/S0009-2614\(98\)00144-4](https://doi.org/10.1016/S0009-2614(98)00144-4).
- [48] N. Woznica, L. Hawelek, H.E. Fischer, I. Bobrinetskiy, A. Burian, The atomic scale structure of graphene powder studied by neutron and X-ray diffraction, *J. Appl. Crystallogr.* 48 (2015) 1429–1436, <https://doi.org/10.1107/S1600576715014053>.
- [49] A.C. Forse, C. Merlet, P.K. Allan, E.K. Humphreys, J.M. Griffin, M. Aslan, M. Zeiger, V. Presser, Y. Gogotsi, C.P. Grey, New insights into the structure of nanoporous carbons from NMR, Raman, and pair distribution function analysis, *Chem. Mater.* 27 (19) (2015) 6848–6857, <https://doi.org/10.1021/acs.chemmater.5b03216>.
- [50] K. Kawasumi, Q. Zhang, Y. Segawa, L.T. Scott, K. Itami, A grossly warped nanographene and the consequences of multiple odd-membered-ring defects, *Nat. Chem.* 5 (9) (2013) 739–744, <https://doi.org/10.1038/nchem.1704>.
- [51] Z. Sofer, P. Šimek, O. Jankovský, D. Sedmidubský, P. Beran, M. Pumera, Neutron diffraction as a precise and reliable method for obtaining structural properties of bulk quantities of graphene, *Nanoscale.* 6 (21) (2014) 13082–13089, <https://doi.org/10.1039/C4NR04644G>.
- [52] A. Eckmann, A. Felten, A. Mishchenko, L. Britnell, R. Krupke, K.S. Novoselov, C. Casiraghi, Probing the nature of defects in graphene by Raman spectroscopy, *Nano Lett.* 12 (8) (2012) 3925–3930, <https://doi.org/10.1021/nl300901a>.
- [53] J.-B. Wu, M.-L. Lin, X. Cong, H.-N. Liu, P.-H. Tan, Raman spectroscopy of graphene-based materials and its applications in related devices, *Chem. Soc. Rev.* 47 (5) (2018) 1822–1873, <https://doi.org/10.1039/C6CS00915H>.
- [54] M. Mermoux, Y. Chabre, A. Rousseau, FTIR and ¹³C NMR study of graphite oxide, *Carbon N. Y.* 29 (3) (1991) 469–474, [https://doi.org/10.1016/0008-6223\(91\)90216-6](https://doi.org/10.1016/0008-6223(91)90216-6).
- [55] J.Y. Cho, J.I. Jang, W.K. Lee, S.Y. Jeong, J.Y. Hwang, H.S. Lee, J.H. Park, S. Y. Jeong, H.J. Jeong, G.-W. Lee, J.T. Han, Fabrication of high-quality or highly porous graphene sheets from exfoliated graphene oxide via reactions in alkaline solutions, *Carbon N. Y.* 138 (2018) 219–226, <https://doi.org/10.1016/j.carbon.2018.06.013>.
- [56] V. Rebuttin, E. Fazio, S. Santangelo, F. Neri, G. Caputo, C. Martin, T. Brousse, F. Favier, N. Pinna, Chemical modification of graphene oxide through diazonium chemistry and its influence on the structure-property relationships of graphene oxide-iron oxide nanocomposites, *Chem. - A Eur. J.* 21 (2015) 12465–12474, <https://doi.org/10.1002/chem.201500836>.
- [57] E. Fuente, J.A. Menéndez, M.A. Díez, D. Suárez, M.A. Montes-Morán, Infrared Spectroscopy of carbon materials: a quantum chemical study of model compounds, *J. Phys. Chem. B.* 107 (2003) 6350–6359, <https://doi.org/10.1021/jp027482g>.
- [58] T. Szabó, O. Berkesi, P. Forgó, K. Josepovits, Y. Sanakis, D. Petridis, I. Dékány, Evolution of surface functional groups in a series of progressively oxidized graphite oxides, *Chem. Mater.* (2006), <https://doi.org/10.1021/cm060258+>.
- [59] Y.C.G. Kwan, G.M. Ng, C.H.A. Huan, Identification of functional groups and determination of carboxyl formation temperature in graphene oxide using the XPS O 1s spectrum, *Thin Solid Films.* 590 (2015) 40–48, <https://doi.org/10.1016/j.tsf.2015.07.051>.
- [60] V. Sridhar, I. Lee, H.-H. Chun, H. Park, Hydroquinone as a single precursor for concurrent reduction and growth of carbon nanotubes on graphene oxide, *RSC Adv.* 5 (84) (2015) 68270–68275, <https://doi.org/10.1039/C5RA09871H>.
- [61] K. Pytlakowska, V. Kozik, M. Matussek, M. Pilch, B. Hachuła, K. Kocot, Glycine modified graphene oxide as a novel sorbent for preconcentration of chromium, copper, and zinc ions from water samples prior to energy dispersive X-ray fluorescence spectrometric determination, *RSC Adv.* 6 (49) (2016) 42836–42844, <https://doi.org/10.1039/C6RA03662G>.
- [62] D.A. Skoog, F.J. Holler, S.R. Crouch, *Principles of Instrumental Analysis, 7th ed.*, Cengage learning, Boston, MA, 2017.
- [63] P. Sharma, M.R. Das, Removal of a cationic dye from aqueous solution using graphene oxide nanosheets: investigation of adsorption parameters, *J. Chem. Eng. Data.* 58 (1) (2013) 151–158, <https://doi.org/10.1021/je301020n>.
- [64] B. Mao, B. Sidhureddy, A.R. Thirupathi, P.C. Wood, A. Chen, Efficient dye removal and separation based on graphene oxide nanomaterials, *New J. Chem.* 44 (11) (2020) 4519–4528, <https://doi.org/10.1039/C9NJ05895H>.
- [65] M. Yin, Y. Pan, C. Pan, Adsorption properties of graphite oxide for Rhodamine B, *Micro Nano Lett.* 14 (11) (2019) 1192–1197, <https://doi.org/10.1049/mna2.v14.1110.1049/mnl.2018.5820>.
- [66] L. Adamčíková, K. Pavlíková, P. Ševčík, The decay of methylene blue in alkaline solution, *React. Kinet. Catal. Lett.* 69 (2000) 91–94, <https://doi.org/10.1023/A:100569626749>.

- [67] W.J. MacNeal, J.A. Killian, Chemical studies on polychrome methylene blue 1, *J. Am. Chem. Soc.* 48 (3) (1926) 740–747, <https://doi.org/10.1021/ja01414a031>.
- [68] N. Yadav, B. Lochab, A comparative study of graphene oxide: Hummers, intermediate and improved method, *FlatChem.* 13 (2019) 40–49, <https://doi.org/10.1016/j.flatc.2019.02.001>.
- [69] Y. Cui, Y.H. Lee, J.W. Yang, Impact of carboxyl groups in graphene oxide on chemoselective alcohol oxidation with ultra-low carbocatalyst loading, *Sci. Rep.* 7 (2017) 3146, <https://doi.org/10.1038/s41598-017-03468-4>.